Vacuum 227 (2024) 113354

Contents lists available at ScienceDirect

Vacuum

journal homepage: www.elsevier.com/locate/vacuum

Planar deposition of Nb thin films by HiPIMS for superconducting radiofrequency applications

Carlota P.A. Carlos [a,b,*], Stewart Leith [a], Guillaume Rosaz [a], Stephan Pfeiffer [a], Carmine Senatore [b]

[a] CERN, European Organization for Nuclear Research, 1211 Geneva, Switzerland
[b] Department of Quantum Matter Physics, University of Geneva, Geneva, Switzerland

ARTICLE INFO

Keywords:
Superconducting radiofrequency cavities
Niobium thin film
HiPIMS
Ion Bombardment
Kinetic Monte Carlo simulations
Planarization

ABSTRACT

Cost efficiency and sustainability are critical challenges for future accelerator machines. Nb-coated Cu (Nb/Cu) superconducting radiofrequency (SRF) accelerating cavities, while requiring R&D to meet high acceleration gradient performance standards, show potential for addressing these challenges. Defects in the Nb layer responsible for the deterioration of cavity performance have been linked to the underlying Cu substrate. This study investigates a novel optimization method by mitigating the substrate surface's impact on deposited Nb, using High Power Impulse Magnetron Sputtering alongside a DC substrate bias (from −50 to −300 V). Trenched silicon substrates are chosen to emulate substrates with exceptionally rugged surface characteristics. Film deposition is investigated both experimentally and through kinetic Monte Carlo simulations. Higher DC voltages are shown to eliminate self-shadowing during the coating process via improved incident ionic flux directionality, enhanced adatom mobility and increased re-sputtering rates, ultimately yielding flat and densely-packed films. The influence of the substrate's shape on the film's surface was found to decrease exponentially with increasing ion bombardment energies. Films sputtered under high DC bias conditions (−300 V) exhibited complete planarization with a 30% re-sputtering rate. Strategies for applying this technique to Nb/Cu SRF cavities, enhancing their viability for future particle accelerators, are also discussed.

1. Introduction

Particle accelerators have proven to be essential devices for fundamental research in high-energy physics (HEP) [1]. The remarkable technological advancements in this field also allowed for the progressive use of accelerators in other applications [2–4]. Across all fields, energy and cost efficiency are driving the technological developments: for HEP experiments, these are key aspects to achieve running feasibility of future machines like the Future Circular Collider (FCC) [5], while cost effective superconducting accelerators, with reduced energy footprint and capital investment, could lead to widespread commercial use of this technology and enable new societal applications [6], for example in domains like isotope production [7] or wastewater treatment [8]. Superconducting radiofrequency (SRF) accelerating cavities, specifically, also hold promise for applications beyond accelerators, e.g. in superconducting quantum sensing [9] and quantum information systems [10].

Together with the associated cryogenic systems, SRF cavities contribute significantly to the overall energy consumption of an accelerator. In FCC-ee, for example, projections indicate that they could account for over 50% of the total electricity consumption [11], currently estimated at an average of 1.4 TWh per year [12]. The optimization of these devices is therefore mandatory to achieve higher cost-effectiveness and sustainability for these machines.

Two primary strategies for SRF cavities are currently being explored: bulk Nb and thin-film superconductors. While bulk Nb is currently the state of the art performance wise, with quality factors (Q_0) exceeding 10^{10} at accelerating gradients (E_{acc}) up to 50 MV/m [13,14], Nb/Cu cavities offer several potential advantages for cost reduction and operational efficiency [15]. Notably, Nb/Cu cavities can operate at higher temperatures (4.5 K vs 2 K for bulk Nb) due to lower BCS surface resistance of the Nb films [16]), allowing for lower cryogenic plant operating costs. Additionally, they exhibit lower sensitivity to the ambient magnetic field [16], simplifying accelerator operation and design, and the higher thermal conductivity of Cu enhances their overall thermal stability at cryogenic temperatures [17]. Moreover, Nb/Cu SRF cavities have already been successfully employed in circular colliders, such as LEP-II [18] and the LHC [19], as well as in linear accelerators such as HIE-ISOLDE [20] and ALPI [21].

* Corresponding author at: CERN, European Organization for Nuclear Research, 1211 Geneva, Switzerland.
E-mail address: carlota.pereira@cern.ch (C.P.A. Carlos).

https://doi.org/10.1016/j.vacuum.2024.113354
Received 10 January 2024; Received in revised form 4 April 2024; Accepted 31 May 2024
Available online 3 June 2024

However, for FCC-ee, SRF Nb/Cu cavities require operational parameters beyond the state of the art. While LHC performance requirements for 400 MHz Nb/Cu cavities at 4.5 K were set to $Q_0 = 2 \times 10^9$ at $E_{acc} = 5.5$ MV/m [22], FCC-ee calls for significantly higher performance. Nb/Cu SRF 400 MHz cavities working at 4.5 K are expected to run with quality factors above $Q_0 = 3.3{\times}10^9$ at $E_{acc} = 6.9$ MV/m, for the single cell configuration in the Z machine, and $E_{acc} = 13.2$ MV/m for the 2-cell configuration [23] needed for the H and W modes. Notably, 2-cell 400 MHz cavities are also being considered for the Z machine, replacing the 1-cell, if the performance targets are validated in time for series production. The possibility of adopting Nb/Cu for the 800 MHz system is also being considered, if the performance targets ($Q_0 = 3.8 \times 10^{10}$) at high field (24.5 MV/m) can be met reproducibly [23,24].

While Nb/Cu SRF cavity technology is a valid alternative to bulk Nb for machines requiring moderately large accelerating fields, up to 10 MV/m, it is not yet competitive for higher gradient applications due to loss mechanisms at high fields — a phenomenon termed *Q-slope* — caused by an increase in thin-film surface resistance with increasing surface magnetic fields. The Q-slope found in LEP-II and LHC cavities [25,26], where the Nb films were deposited by DC magnetron sputtering (DCMS), was attributed to defects within the deposited layer [27,28,22]. To address this issue, CERN adopted a multifaceted approach. From the experience with HIE-ISOLDE [29], electron beam welding was replaced with seamless fabrication techniques, eliminating defect-inducing welds at the equator of the Cu substrates. In parallel, the electropolishing of the Cu substrates was implemented to further improve the substrate quality.

Finally, a different coating technique, High Power Impulse Magnetron Sputtering (HiPIMS), was proposed and found to densify the growing thin film [30], due to the production of metal ions that can be accelerated toward the substrate. The velocity at which the ions impinge the substrate and the growing film, and therefore the ion bombardment energy, depends directly on the applied DC bias voltage, unlike in DCMS, where particle energy is controlled mainly by the deposition pressure. This allows for much higher impinging energies compared to DCMS, which in turn results in denser, defect-free films. Nb films on Cu deposited with HiPIMS were optimized first on small samples measured with the quadrupole resonator (QPR) and on TESLA shape 1.3 GHz single cell cavities. Experimental results for Nb/Cu films deposited by HiPIMS onto QPR samples indicated residual surface resistances similar to those of the state-of-the-art bulk Nb, with significant Q-slope mitigation [31]. When combined with appropriate surface treatment and seamless substrates, Nb films with bulk-like behavior were achieved on 1.3 GHz resonators, with Q_0 above 2×10^{10}, up to E_{acc} around 10 MV/m at 1.7 K [32]. Furthermore, recent results on a 400 MHz single cell cavity coated with bipolar HiPIMS showcased a much improved Q-slope when compared to a previous DCMS coating on the same substrate, closely aligning with the FCC-ee Z-pole single-cell target [33], despite using non-optimized substrate, substrate treatment, and coating parameters.

While recent breakthroughs and record RF performances demonstrate the immense potential of HiPIMS for high-performance Nb/Cu cavities, these cavities still fall short of the demanding requirements set for FCC-ee at this stage of their technological development. One route for further optimization could be to disentangle the thin-film morphology from that of the substrate: defects on the deposited layer can arise from the substrate, as thin films replicate the surface state of the substrate onto which they are deposited. Thus, the roughness of the substrate has a strong influence on the roughness of the film. Rougher films with poorly connected Nb film grains can experience losses under RF field, possibly due to losses in weak-links [22] or easier penetration of (Josephson) fluxons [34]. Previous studies performed with different substrate roughnesses (hydroformed, spun and electroplated Cu cavities), also demonstrated that smoother substrates led to lower residual losses [28].

The aim of the preliminary investigation described in the present contribution is to assess the potential of the HiPIMS technique, combined with a DC substrate bias, to produce Nb layers with a surface morphology independent from that of the underlying substrate. Homma et al. [35] reported a noteworthy technique, achieving planar aluminum films sputtered onto trenched SiO_2 substrates through substrate biasing. This approach successfully eliminated self-shadowing effects during the coating and produced dense films with uniform step coverage of the substrate.

This work aims to evaluate the impact of the incident ion bombardment energy on surface planarization and substrate coverage in HiPIMS coatings. First, 3D kinetic Monte-Carlo simulations are conducted to model the growth of Nb films on trenched Si substrates at multiple ion bombardment energies. Subsequently, the deposition of Nb films by HiPIMS on trenched Si samples, cut from Si-wafers and etched using Focused Ion Beam (FIB) milling, is detailed for different DC substrate bias, ranging from −50 to −300 V. The choice of Si-wafers as the substrate material, as opposed to Cu, is driven by their advantageous properties, such as an extremely flat surface and ease of pattern engraving (compared to Cu [36]), making them a reliable medium for this investigation. The morphology of the films is examined using FIB and Scanning Electron Microscope (SEM) techniques. Film planarization is quantified for each ion bombardment energy. Re-sputtering rates are also calculated for each ion energy. Finally, a potential strategy for the implementation of this technique in SRF cavities is discussed.

2. Simulations

To predict the effect of the ion bombardment energy on the planarization of a Nb layer deposited onto a textured substrate, several Nb films were simulated with NASCAM (NAnoSCAle Modeling [37], version 4.6.X). This 2D-3D Kinetic Monte Carlo modeling software simulates the deposition, diffusion, nucleation and growth of films on a surface by a ballistic approximation. Particles are considered to be hard spheres, randomly ejected towards the substrate along linear trajectories according to their energy and angular distribution. Once they reach the film surface, different mechanisms and surface mobility

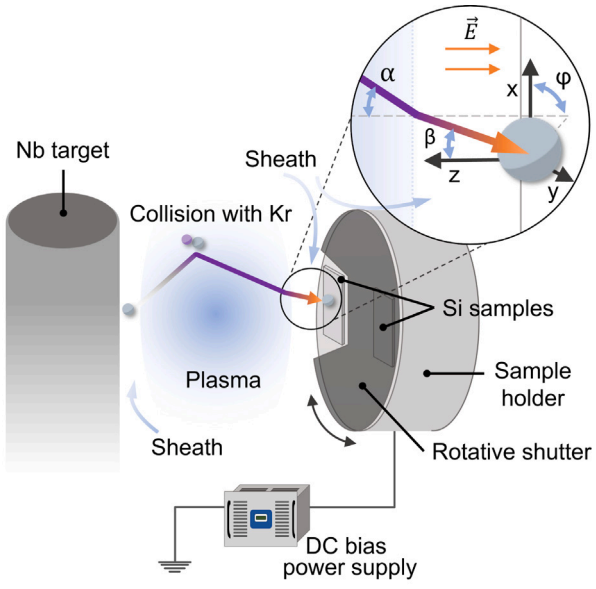

Fig. 1. Schematic illustration of the experimental setup (side view), with a close up highlighting the incidence plane, the coordinate system, and the electrical field direction. The deflection effect of the Coulomb force within the plasma sheath on the ionic incident angle in relation to the surface normal, $\beta < \alpha$, is also depicted.

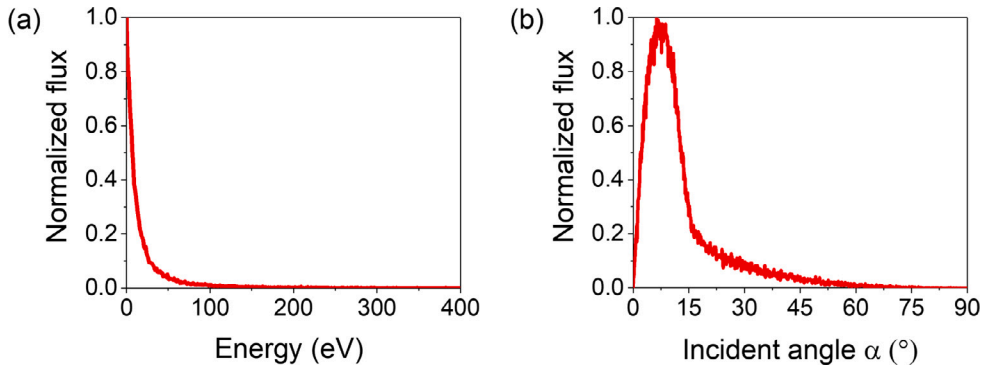

Fig. 2. Energy (a) and (b) angular distribution of the deposited Nb neutrals, simulated through SIMTRA.

processes are possible, depending on the incident energy of the particles, local bond structure, and the process temperature, explained in detail in [38,39].

The energy transferred from incoming Nb ions to the substrate and the atoms in the growing film is computed using a binary collision approximation. Within NASCAM, atomic displacement is considered, favoring movement to energetically more advantageous, empty neighboring lattice sites (both nearest and next-nearest neighbors). This occurs when the energy transferred from the projectile particle to a Nb atom in the film exceeds the surface binding energy of the adatom. However, if neighboring sites are already occupied by other particles, the recoil particle remains at its initial site. The particles are then either redeposited on the substrate with a unity sticking coefficient or removed from the system.

The simulation model has some notable limitations. It does not consider scenarios where recoiling Nb particles, post-collision, have enough kinetic energy to displace subsequent adatoms, potentially initiating collision cascades. Additionally, once a recoiling Nb particle is removed from the system, it is not reintroduced into the simulation dynamics and is incapable of interacting with other Nb particles in the growing film, thus excluding the possibility of re-sputtering. Given the incident ion energies in the hundreds of eVs reported in this work, the absence of re-sputtering in the simulation model stands as a significant limitation, as re-sputtering plays a crucial role in film formation [35,40]. Additionally, the model cannot account for grain evolution, and it assumes the growth of a single, large amorphous grain. It does not consider stress effects, nor the mechanical properties of the growing film. Nonetheless, the model adopted can still be used to understand the influence of the applied DC substrate bias and the ionic impinging energy on film morphology and planarization. The number of deposited particles was selected to ensure it exceeded at least twice the height of the trenches, as done experimentally. The coating temperature of the films (423 K) is negligible when compared to the melting temperature of Nb (2750 K), leading to little adatom surface mobility [41,40,42]. Thus, diffusion is neglected in the simulations. To shorten the computational times, film growth dynamics with the working gas were also not considered. The same reasoning stands for bypassing the effect of the double-ionized species, as they have a lower contribution to the ionization flux [30].

For the simulation of the Nb growth on a textured substrate, a 3D lattice approach was adopted. Making use of a pre-existing plugin of NASCAM, a 40 × 5 × 6 nm^3 rectangular substrate (corresponding to 400 × 50 lattice nodes), with 3 periodically spaced 5 × 5 nm^2 trenches, was created. The total number of deposited particles (comprising atoms and ions) amounted to 2 × 10^6, which is equivalent to 100 monolayers of Nb, or an effective sample thickness between 10 to 14 nm. It is important to note that the simulated trenches are significantly smaller than those created experimentally by FIB milling, mainly due to computational memory constraints (no computing cluster available). The atomic displacement energy and the substrate binding energy were set to 7.59 eV and 4.7 eV, respectively, corresponding to the heat of sublimation energies of Nb and Si [43].

The particle flux in our system consists of atoms (neutrals) and ions, each with distinct energy and angular distributions. To determine these distributions for neutrals, SIMTRA (SImulation of Metal TRAnsport [44–46]) simulations tailored to our experimental configuration and process conditions were conducted. The calculations were based on binary elastic collisions with the process gas (Kr) atoms in the chamber. Fig. 1 provides a simplified schematic representation of our coating configuration, while a more comprehensive description can be found in Appendix. Detailed information about the coordinate system used is also included.

The input nascent angular and energy distributions of Nb sputtered atoms leaving the target were obtained from SRIM (The Stopping and Range of Ions in Matter [47,48]) calculations. To create the particles' starting positions, a racetrack profile with rotatable symmetry was employed, fitted to match the experimental erosion profile of the Nb target. A Molière screened Coulomb potential was used to model the Nb-Kr interaction. The resulting energy and angular distributions are depicted in Fig. 2. Notably, the angular distribution has a Full Width at Half Maximum (FWHM) of approximately 11 degrees.

The energy distributions of the ions in the particle flux were modeled as monoenergetic beams, as E_{ion} is determined by the absolute value of the DC substrate bias voltage U_B, $E_{ion} = e \times U_B$ (eV) [49,50]. Considering the range of U_B values considered, which spans from −50 to −300 V, E_{ion} falls within the 50 to 300 eV range. With electron impact ionization as the dominating ionization mechanism for HIPIMS processes [51], the original momentum of the sputter-ejected neutrals is conserved in the ionization event and both neutrals and ions (sputtered as neutrals from the same location of the target and ionized en route to the substrate) are assumed to arrive at the plasma sheath[1] with the same incidence angle α.

The potential drop along the surface normal between the plasma sheath entrance and the substrate, which is negatively biased, creates an electric field that accelerates the ions in the sheath, as represented in Fig. 1, such that the difference between the incident and initial kinetic energy is equal to the potential energy provided by the DC bias,[2] U_B,

$$\frac{1}{2}mv_z^2 - \frac{1}{2}mv_{z0}^2 = eU_B, \tag{1}$$

[1] A thin, non-neutral layer of plasma that forms at the boundary between the bulk plasma and the negatively biased substrate.

[2] This is only valid for a collisionless sheath. At 2.3 × 10^{-3} mbar (the deposition pressure), the mean free path for ion collisions with Kr molecules is in the cm range (calculated as in ref [52]), which is typically larger than the sheath width for our range of substrate bias [53] calculated through Child's Law (below 1 cm). With this simplified classical treatment, the sheath can thus be considered collisionless.

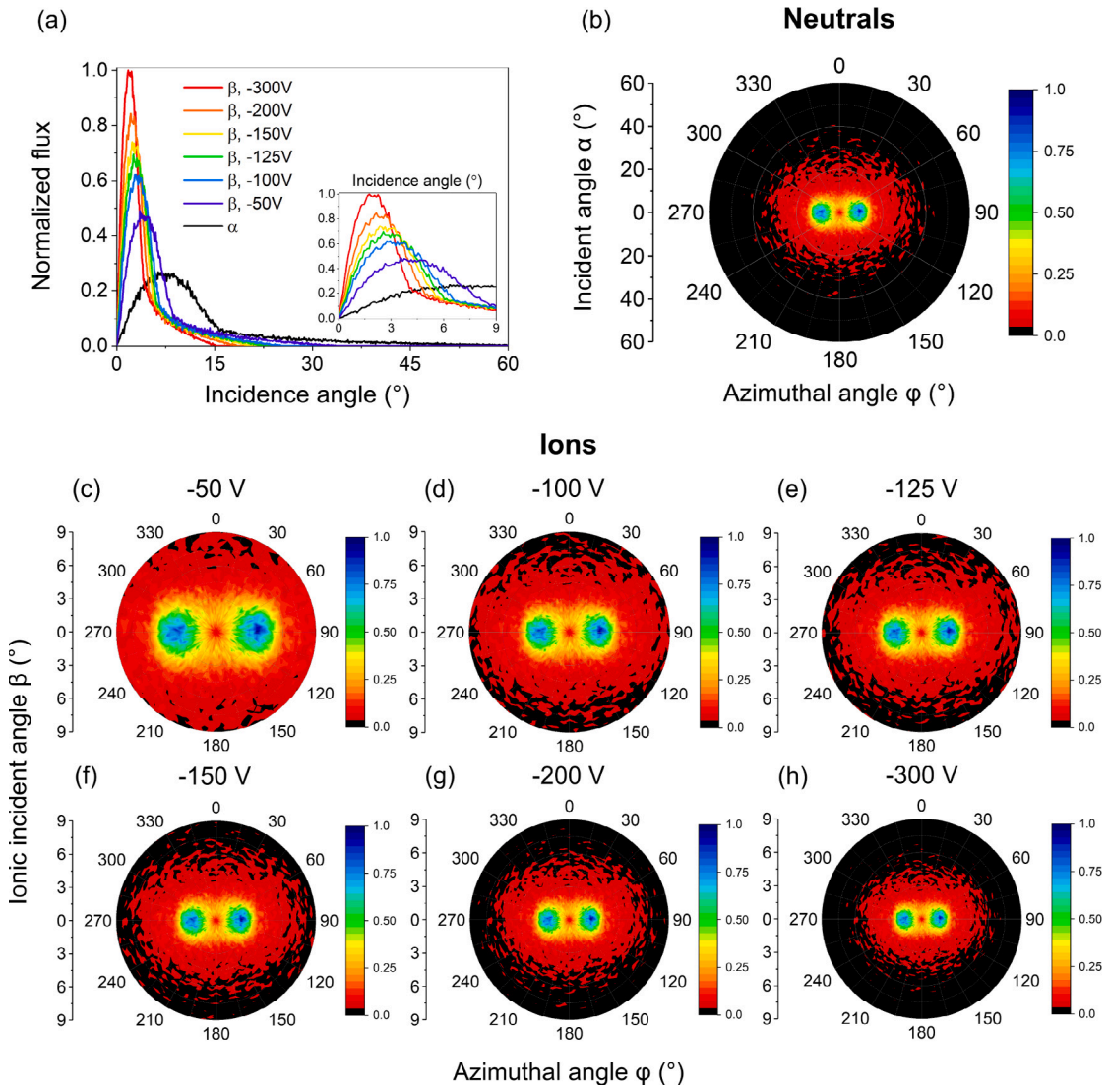

Fig. 3. (a) Angular distribution of the Nb particles incidence angles relative to the surface normal: α for neutrals, computed using SIMTRA, and β for ions under the specified DC bias values calculated via Eq. (4), ranging from −50 to −300V. The inset provides a detailed view of the ionic distributions and their response to increasing DC voltage values, highlighting its narrowing effect on the FWHM. Polar plots illustrating the angular distribution on the incidence plane are shown in panels (b) through (h), with (b) depicting neutrals, and panels (c) to (h) portraying the ionic angular distribution of the different substrate bias values used. The intensity scale of each plot is normalized to the maximum flux in each configuration. The effect of increasing the DC substrate bias is evident in the progressive narrowing of the angular distributions. Ion trajectories are unaffected in ϕ, as the Coulomb force acts solely on the surface normal plane.

e and m being the ion charge and mass, and v_{z0} and v_z the initial and incident velocity along the surface normal. Therefore, v_z can be expressed as

$$v_z = \sqrt{v_{z0}^2 + \frac{2eU_B}{m}}. \tag{2}$$

Considering the parallel component of the incident velocity,

$$v_x = v_{x0}, \tag{3}$$

and that $v_{z0} = v_0 cos(\alpha)$ and $v_{x0} = v_0 sin(\alpha)$, the angle of ionic incidence β upon reaching the substrate can be computed in correlation with the angle of incidence at the sheath entrance α, which also corresponds to the angle of incidence for neutrals at the substrate (since they remain unaffected by the bias):

$$\tan^2(\beta) = \frac{v_x^2}{v_z^2} = \frac{1}{1 + \frac{U_B}{E_0}} \tan^2 \alpha, \tag{4}$$

with E_0 representing the mean initial energy of the ions when entering the sheath, equal to the weighted average energy of the neutrals (~20 eV). Hence, the Coulomb force created by biasing the substrate deflects all ions along the surface normal, resulting in an incident angle β such that $\beta < \alpha$.

The incident angular distributions calculated through Eq. (4) for the Nb ions for the different substrate bias considered are shown in Fig. 3(a), with the previously calculated angular distribution of the neutrals α of Fig. 2(b) superimposed in black for easier comparison. The effect of the DC substrate biases on the incident angular distribution of the Nb ions is clearly visible — the ion direction upon impact is determined by the sheath potential, that forces a directional ion bombardment normal to the surface. Higher values lead to increasingly higher deflections, resulting in increasingly narrower, normal-oriented distributions, as highlighted on the inset of Fig. 3(a). To further describe the impinging particle flux, polar plots with the angular distribution in the incidence plane are shown in Fig. 3(b) for neutrals, and ions, Figs. 3(c)–(h).

In Fig. 3(b), the polar plot showcases the incident angle α plotted against the azimuthal angle ϕ for arriving Nb neutrals, calculated using SIMTRA. The intensity scale, normalized to the maximum flux, provides

insights into the probability of incidence. The two symmetrical regions highlighted in green and blue, centered around azimuthal angles ϕ = 90° and ϕ = 270° (with ±30° of dispersion), with α angles between 9°±5.5°, correspond to where the probability of arrival exceeds 0.5. The rest of the impinging particle flux is dispersed around these two regions, with decreasing probability, radially along α. Considering the selected geometry, illustrated in Fig. 1, where the sample surface aligns with the ϕ plane, it becomes evident that the majority of the particles arrive from either the right (around ϕ = 90°) or the left (around ϕ = 270°) sides of the chamber, most likely due to the collisions with the Kr gas.

Figs. 3(c) to (h) show the angular distribution at the incident plane of the Nb ions in the case of the different DC bias values applied to the substrate, from −50 to −300 V. The Coulomb force created by the bias is only acting along the surface normal, so the ion trajectories suffer no alteration in ϕ when entering the sheath. Therefore, the only difference between the multiple ion polar plots comes from the higher deflection induced by the Coulomb force when increasing the applied bias: the incident ions impinge the surface closer and closer to the surface normal with increasingly narrower distributions, reaching mean β angles with the normal as low as $\approx 2.0° \pm 2.9°$, for -300 V of bias. The angular distribution of incident atoms α can be effectively approximated by a cone with a FWHM of around 11°. Based on Eq. (4), it becomes evident that the ions' angular distributions β are confined within increasingly narrower cones with increasing ion bombardment energy, exhibiting FWHM values ranging from 6° to 3° (for the lowest and highest bias, respectively). Consequently, this leads to a shrinkage of the incidence cone with respect to the surface normal, compared with the case of no bias, amounting to approximately 44% for −50 V, 57% for −100 V, 61% for 125 V, 64% for −150 V, 68% for −200 V, and 74% for −300 V.

Finally, to simulate film growth, it is necessary to quantify the fraction of the sputtered metal atoms that become ionized in the plasma. This property was not measured for our operational parameters and sputtering system. The reported ionized flux fraction for metals in HiPIMS spans the range from about 10% to over 80% [54,55], depending on the target material and process conditions. The reported results are sometimes inconsistent, due to the difficulty of the measurement itself and the multiple magnetron configurations and applied power densities. For Cu HiPIMS discharges, for example, Kozák et al. [56] estimated an ionization probability of 64%–75%. Similar modeling efforts have estimated ionization probabilities of 65%–70% for Al [57], and 92% for Ti [58]. Based on results reported in the literature for Nb [59–61], and given that this material has an ionization potential in the range of the above mentioned metals, an ionization fraction of 70% was considered as a fair approximation and is used in our study. This value is considered constant and is independent of the biasing voltage used (depends only on the power density supplied to the target [62]).

3. Material and methods

Pure Nb films were deposited by HiPIMS on 10 × 20 mm Si samples, cut out from 4" phosphorus-doped, (100)-oriented Si-wafers, exhibiting a resistivity of 0.001–0.005 Ω cm. Prior to their coating, 20 μm-long, 1x1 μm trench-like profiles were engraved on the samples by FIB direct milling. Each sample was ultrasonically cleaned with commercial acetone and ethanol before the milling and then again prior to the coating processes. The coated samples were then analyzed by FIB cross-section preparation and SEM imaging. The same experimental apparatus, processes, and parameters hereafter described were maintained for all samples, with the exception of the parameter of interest — DC bias voltage applied during the HiPIMS coating — that ranged from −50 to −300 V.

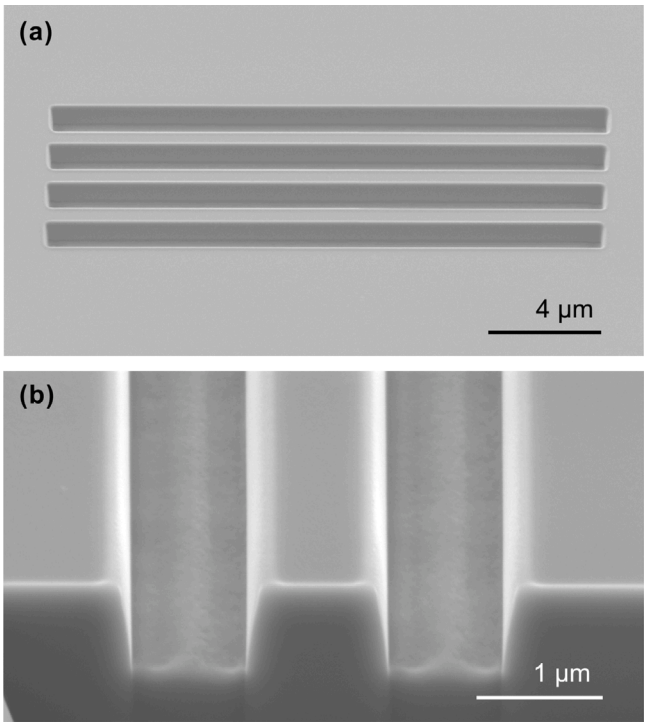

Fig. 4. SEM micrographs of (a) the top surface and (b) cross section of a trenched Si sample following FIB milling.

3.1. FIB milling

The engraving of trenches on the Si wafers was performed with a Zeiss Crossbeam 540 FIB-SEM system, equipped with a Field Emission Gun (FEG). Employing an accelerating voltage of 30 kV and a current of 100 pA, trenches measuring 1 × 1 × 120 μm were successfully engraved with Ga^+ ions onto the Si substrates.

Trial samples were then analyzed by SEM and FIB cross sectional milling, as shown in Fig. 4(b), allowing for the visual inspection of the trenches' profile. These cross sectional cuts were performed with Ga^+ using an accelerating voltage of 30 kV and currents of 700 pA and 300 pA, up to a depth of 5 μm. The Secondary Electron Secondary Ion (SESI) and In-Lens detectors were used for imaging of the resulting cross sections as they provided the greatest electron contrast. The milled structures' geometry remains imperfectly square due to some Si re-deposition on the structure walls during the engraving process. This distortion rounds the trench sides and creates a slight bump at the bottom. The engraved samples to be coated with Nb were not analyzed by FIB cross-sections prior to coating, as this process damages the trenches.

3.2. HiPIMS coatings

Following the milling, the samples were placed in pairs on two sample holders, meaning a total of 4 samples were coated per coating run. Each holder was equipped with a shutter to isolate in turn the to-be-coated sample. The holders were mounted on an Ultra-High-Vacuum (UHV) stainless steel chamber, diametrically opposing each other. The chamber was subsequently connected to a sputtering system whose configuration is detailed in Appendix. Both assemblies were performed inside an ISO5 cleanroom.

The entire system was then transported to the coating bench where it was coupled to the UHV pumping group and gas injection lines, and pumped down to about 1×10^{-7} mbar. At this point, a leak check was performed, before starting a 200°C, 48h-long, bakeout of the pumping

Table 1
Summary of the HiPIMS coating parameters.

Pulse duration (μs)	200	Sputtering gas	Kr
Frequency (Hz)	100	Sputtering pressure (mbar)	2.3×10^{-3}
Average power (kW)	1.2	Coating temperature (°C)	150
Peak current (A)	170	Coating duration (h)	2
Bias voltage (V)	−50, −100, −125, −150, −200 &−300		

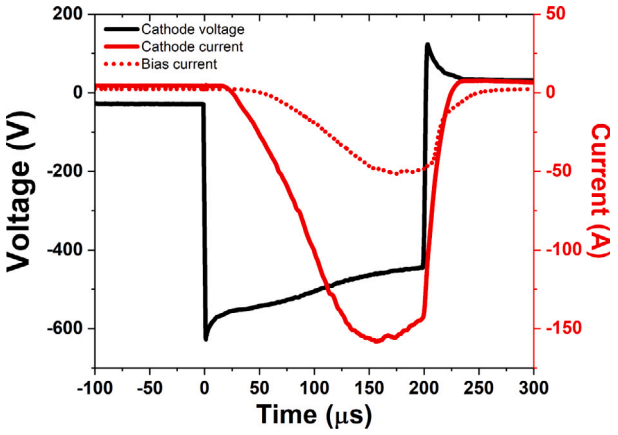

Fig. 5. Voltage (black) and current (red) waveforms of a typical HiPIMS discharge using the parameters detailed in Table 1, with applied DC bias voltage of −75 V.

group and the coating apparatus. A Non-Evaporable Getter (NEG) pump connected to the sputtering system was activated for 4 h just before turning off the bakeout. After cooling down, the system reached a base pressure of $\approx 2 \times 10^{-9}$ mbar. Deposition under UHV minimizes oxygen and hydrogen contamination in the sputtered Nb films. While the rest of the system cooled down after the bakeout, the samples themselves were maintained at a higher temperature of 150°C until the coating began.

Prior to coating, ultra-pure krypton (99.9999%) was injected into the system until a process pressure of 2.3×10^{-3} mbar was reached. At this point, the heating of the UHV chamber with the samples was stopped. HiPIMS coatings were performed with the parameters shown in Table 1 for a duration of 2 h per sample, to ensure sufficiently thick layers (~2 μm). During the coating process, the temperature of the samples was carefully monitored. An infrared thermal sensor (OMEGA OS100-SOFT) was used for this purpose. To maintain a constant temperature of 150 °C, a fan was employed. The plasma discharge was maintained using a pulsed power supply (Huettinger TruPlasma HighPulse 4006) and the negative substrate bias voltage was applied to the samples using a DC power supply (Huettinger TruPlasma Bias 3018). The central electrode was connected to the power supply while the upper and lower electrodes were grounded, acting as anodes during the plasma discharge, which allowed the DC biasing of the chamber (and therefore the substrates) at the desired potentials. The discharge and bias voltages and currents were monitored throughout the entire coating process using voltage (Tektronix P6015 A) and current (Pearson current monitor 301×) probes whose signals are recorded by a digital oscilloscope (Picoscope 2000). A snapshot of a typical discharge is given in Fig. 5. After each coating, the samples were cooled down to room temperature, after which the chamber was vented with a gas mixture of N_2O_2 (N_2 80% + O_2 20%).

3.3. Sample characterization

The Nb-coated Si samples were analyzed via SEM imaging of a series of FIB cross section cuts through the previously engraved areas of the samples. The same Zeiss Crossbeam 540 FIB-SEM system as previously reported was used, following the procedure and parameters established during the evaluation of the milling process.

4. Results

In this section, the findings of the NASCAM simulations are presented first, followed by the experimental results. To help quantify the influence of ion bombardment energy on film planarization, the peak heights are calculated and normalized to their maximum value for both simulations and experimental results. Additionally, the effect of re-sputtering is assessed by determining the re-sputtering rates for each ion energy.

4.1. NASCAM simulations

Nb layers deposited onto trenched Si substrates were simulated in NASCAM for different ion bombardment energies, 50 to 300 eV. Cross-sections of the simulated Nb films are shown in Fig. 6(a) to (f), where the results are labeled by the corresponding DC substrate bias for which they were simulated.

These film cross sections were generated using a computational code in *Matlab*. The code created 2D particle location histograms based on the 3D NASCAM-simulated films. It achieved this by sampling successive slices of (X, Z) planes along their Y axis. The resulting histograms are displayed in greyscale, where black represents the minimum value, indicating no atoms were deposited in that location along the film, and white represented the maximum value, signifying consistent particle deposition across all sampled (X, Z) planes. To enhance clarity, Si substrates are highlighted in gray, to make them easily distinguishable from the film.

The simulated Nb films showcase extreme differences. At lower ionic energies, 50 and 100 eV (−50 and −100 V of DC substrate bias, respectively), Fig. 6(a) and (b), the film grows in columnar structures on the top and bottom of the trenches, with sharp crevices where these structures meet. As the ion bombardment energy increases, Figs. 6 (c) to (f), these crevices smooth out and the Nb columns connect to each other on top of the grooves — the joining of the islands and the formation of a continuous film occurs sooner (at smaller thickness) with more intensive ion bombardment. The degree of surface planarization seems to increase in proportion to the increase in bias value, as does the density of the films (less porosities and gaps). At about −300 V, Fig. 6(f), the film is significantly flatter and much less porous than at −50 V. The gap between the film and the side walls inside the trenches, however, keeps increasing with increasing ion bombardment energy. From −150 V onwards, voids covered by and with no connection to the overhanging film are visible, growing bigger with increasing ionic energies. This is believed to be an artifact induced by the simulation model used, and will be discussed in detail below in the discussion section.

4.2. HiPIMS Nb/Si films

The influence of the ion bombardment energy on film planarization was then experimentally evaluated by depositing a thin Nb film on top of the FIB-trenched Si samples (Fig. 4) at multiple DC substrate bias, from −50 to −300 V (*i.e.*, ion bombardment energies 50 to 300 eV). The samples were then analyzed through SEM imaging of FIB cross sections, which are presented in Fig. 7(a) to (f).

Observing the cross sections of the deposited films, the planarization effect predicted by the NASCAM simulations at higher DC substrate bias values is also present. The films become progressively flatter the higher the ion bombardment energy during their deposition. Indeed, the film's surface appears notably smoother when coated with the highest substrate bias of −300 V, as shown in Fig. 7(f). Higher film densification in the trenches is also visible at the higher DC substrate bias voltages, −200 V and −300 V, Fig. 7(e) and (f), respectively, where the small voids visible in the films coated at lower values disappear completely. The larger features observed in trenches two and four (from left to right) of sample −50 V are more likely to be caused by dust particles, present on the sample's surface during the coating process, rather than being large voids (different contrast and internal texture).

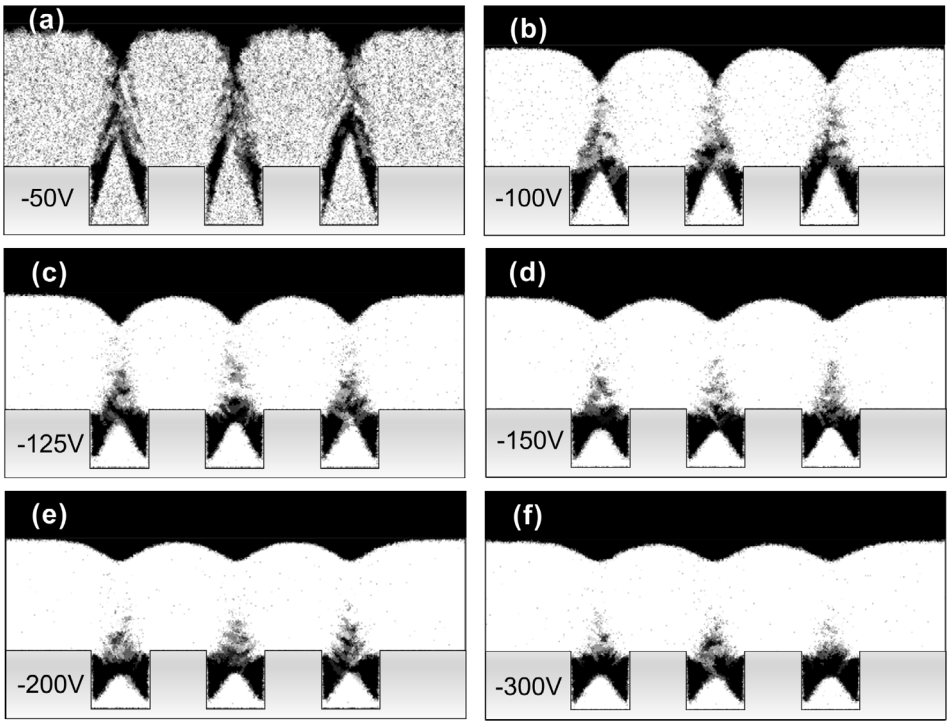

Fig. 6. Cross-sectional views of simulated Nb films emulating HiPIMS coatings, each corresponding to distinct DC substrate bias values: (a) −50, (b) −100, (c) −125, (d) −150 (e) −200, and (f) −300 V. The trenched Si substrates are shaded in gray for clear differentiation from the films.

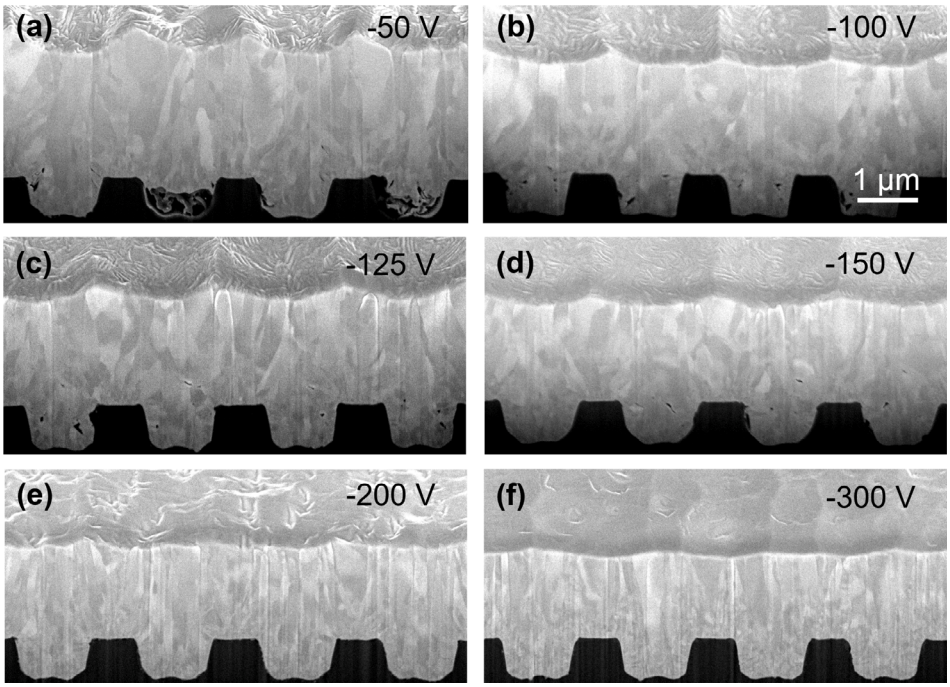

Fig. 7. SEM images of the FIB cross sections of the Nb HiPIMS coatings on a trenched Si substrate at different DC substrate bias voltages: (a) −50, (b) −100, (c) −125, (d) −150, (e) −200, and (f) −300 V. The scale of all 6 pictures is overlaid in (b).

4.3. Normalized peak heights and re-sputtering rates

The effect of ion bombardment energy on the film's surface state was further evaluated for both the simulated and deposited films. The average peak heights at the multiple ion bombardment energies were calculated from Figs. 6 and 7, respectively, resorting to the image processing program ImageJ. These were determined by subtracting the average film thickness at its lowest points, $|t_{base}|$, from the average film thickness at its highest points, $|t_{peak}|$,

$$|\text{peak height}| = |t_{peak}| - |t_{base}|, \quad (5)$$

measuring from a reference height at the top of the trenches, as illustrated in Fig. 8. For the simulated results of Figs. 6, 3 trenches were evaluated, resulting in 2 t_{peak} and 3 t_{base} measurements. For the deposited films, 3 t_{peak} measurements were taken, together with

4 t_{base}. As for Fig. 7(f), the peaks appear shifted to the top of the trenches compared to the other figures, so 4 t_{peak} and 3 t_{base} were measured. In this case, the peaks seem to be dictated by the natural surface roughness of the HiPIMS film, rather than by the influence of the substrate trenches, as is the case of the films coated with lower biases. It is worth noting as well that a potential bias can be introduced in the estimation of peak heights with higher DC substrate bias, as peak positions become less distinguishable. The average peak heights were then normalized to the maximum peak height, i.e., the one found for the lowest ion bombardment energy of 50 eV.

The normalized peak heights, shown in Fig. 8, decrease substantially with increasing ion bombardment energies for both simulated and experimental data. Both data sets are in reasonable agreement. Nonetheless, when it comes to simulated films, no reduction in the normalized peak height is seen between the ion energies of 200 to 300 eV, consistent with what can be observed in Figs. 6(e) and (f), where no visual difference in peak height is found. In contrast, the experimental results reveal a reduction in the normalized peak height between the films deposited at 200 and 300 eV of ion bombardment energy, which corresponds to the reduction in surface roughness verified by the SEM images of the FIB cross sections of Figs. 7 (e) and (f). Furthermore, the experimental trend in normalized peak heights *versus* ion bombardment energy can be described by an exponential decay function (dotted red line in Fig. 8).

As mentioned previously, the algorithm does not account for re-sputtering. To quantify its impact in the growth of our films, the re-sputtering rates for each ion bombardment energy under study were calculated according to

$$\text{re-sputtering rate } (\%) = \frac{D_N - D_B}{D_N} \times 100, \tag{6}$$

where D_B and D_N correspond to the deposition rates with and without substrate biasing, respectively [35]. D_B was calculated for each value of DC substrate bias under consideration, and a HiPIMS-deposited film with no DC bias applied to the substrate (but maintaining the same deposition parameters) was used to estimate D_N. The calculated re-sputtering rates for each ion bombardment energy are displayed in Fig. 9, with values ranging from 7% (50 eV) to 30% (300 eV). Similar values between 6% (50 eV) and 34% (250 eV) can be calculated for Nb films deposited via biased-HiPIMS on Cu substrates, as reported in [63] and plotted in Fig. 9.

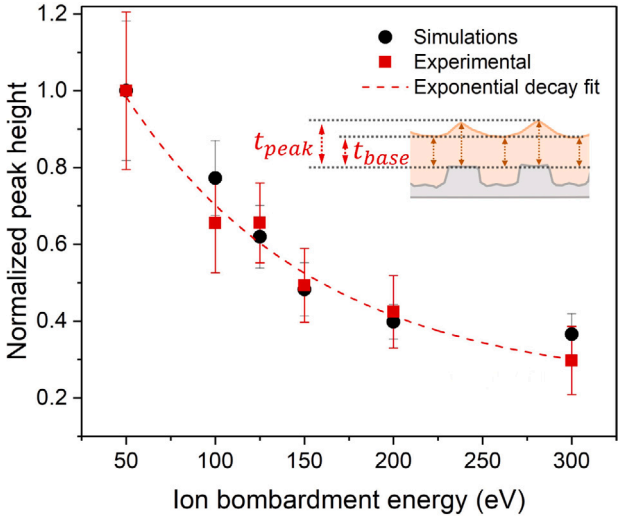

Fig. 8. Normalized peak heights calculated for each ion bombardment energy, with the NASCAM-simulated data in black and the HiPIMS-deposited films in red. The peak heights were normalized relative to the maximum peak height observed at 50 eV. The normalized peak heights seem to decay exponentially with the ion bombardment energy (red dashed line). The inset provides a visual representation of the calculation process for t_{peak} and t_{base}.

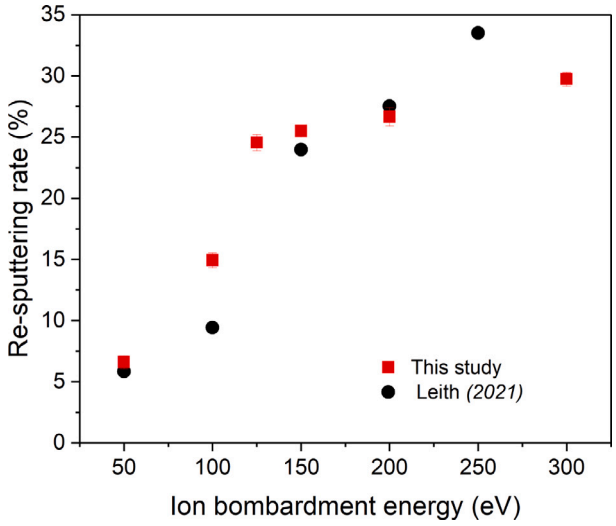

Fig. 9. Re-sputtering rate *versus* ion bombardment energy of the Nb films deposited using the HiPIMS technique as presented in this work, highlighted in red. For comparative purposes, the re-sputtering rates calculated for Nb films deposited onto Cu substrates using HiPIMS and reported in [63] are superimposed in black.

5. Discussion

Historical issues with cavity performance, stemming from the interplay between thin film morphology and substrate properties, prompted an investigation using the HiPIMS deposition technique with DC substrate biasing to try to deposit flat, dense and defect-free Nb films, independent of the substrate's morphology. If proved successful, this approach could prevent the transfer of macro-defects from the substrate to the deposited layer (like the substrate's surface roughness, or point defects such as dents or scratches), potentially boosting cavity performance.

The biased-HiPIMS deposition process was simulated and tested experimentally for different DC substrate bias values. Both NASCAM-simulated and HiPIMS-deposited Nb films were visually confirmed to become subsequently denser and have higher degrees of planarization at higher ionic bombardment energies. This planarization effect was quantitatively analyzed by calculating normalized peak heights for each ion energy, in both the simulated and deposited films, revealing a consistent decrease with rising ion energies, with good agreement between the two data sets. In the case of the HiPIMS-deposited films, an exponential decay relation with increasing ion bombardment energies was identified.

The major difference identified between the simulations and the deposited films was the consistent presence of huge voids within the trenches in the case of the former for all ion bombardment energies considered. This is because the simulated films, while benefiting from the increased directionality of the incident flux and some adatom mobility provided by the higher impinging energies, were not grown assuming re-sputtering. Consequently, the deposition in the NASCAM simulations is extremely influenced by shadowing from previously deposited atoms — self-shadowing — which is the mechanism responsible for the gap formation inside the trenches. Furthermore, the simulation model does not incorporate atomic-scale heating and defect annihilation that occurs at higher bombardment energies, due to the release of potential energy that causes a post-ballistic thermal spike. Their absence in the model likely contributes to the observed discrepancies between simulated and deposited films, such as the presence of voids. The overestimation of voids is further exacerbated by the size difference between the simulated trenches and those produced through FIB milling. Unlike the HiPIMS-deposited films, the normalized peak heights in the simulated films remained constant when increasing the

energy from 200 to 300 eV. This likely stems from the limitations of the simulation model as well.

In Jablonka et al. [64], the public domain NASCAM version was expanded to account for re-sputtering in biased-HiPIMS trench-filling simulations (with Cu and Co). They reported a uniform and dense coverage of the holes in simulations at higher ion energies (200 eV, 80% ionization fraction), which confirms our hypothesis. Re-sputtering, especially from the edges of the opening, improves transport of atoms into the valleys and impedes the formation of pyramids at the bottom of the trench (atoms re-sputtered from there are redeposited on the walls), reducing overhang formation as the film grows. This results in a through coating of the trenches, thus aiding to minimize height variation and surface roughness. Re-sputtering rates between 7% and 30% were found experimentally in this work, so already at 50 eV a reduction in roughness is expected when compared to a non re-sputtering scenario, as is the case of the film simulated at the same energy.

Experimentally, by applying a DC bias of −300 V on the substrate, a flat and dense Nb film was produced, with almost no traces of the substrate's surface state. This results from the simultaneous enhancement of both the alignment of the bombarding ion flux with the surface normal and the re-sputtering rate. The planarization effect is achieved mainly by re-sputtering and the normal incidence of the bombarding ions. The first effectively removes material as the film is growing, which results in the film growing flat along the trenches, while the increased normal incidence contributes to layer densification. The flatness achieved is particularly remarkable due to the ratio between the trench depth and the coating thickness. The aforementioned result demonstrates these two effects to be determinant for planar, dense coatings, further reinforcing the potential of the HiPIMS technique, combined with DC biasing, for the coating of complex substrates when compared to conventional deposition methods like DCMS, and, ultimately, for SRF cavity technology.

Nonetheless, it is necessary to also take into account the consequences of high incident ionic energies on the growing layer itself. The impact of the energetic particle bombardment initiates an interplay between competing processes of defect generation and annihilation: while the kinetic energy leads to displacement and defect creation, followed by re-nucleation, the release of potential energy and the subsequent thermal spike post-collision induces atomic-scale heating, ultimately resulting in defect annihilation [40]. In a Nb/Cu SRF cavity coated with such a layer, the defects created would act as pinning centers for flux trapping, potentially leading to a sufficient degradation of its RF performance to counteract the improvement gained from erasing the influence of the substrate on the film. Higher incident ion energies than 300 eV were not considered for this reason — the flatness achieved at this energy was deemed sufficient and, given the seemingly exponential decay behavior of the normalized peak heights (Fig. 8), the small gain in planarity at even higher ion energies would probably not be significant enough to justify the potential increase in defect density.

In light of these considerations, one approach to prevent the formation of defects at the film's surface, by mitigating the substrate's influence on the Nb film, could involve a two-step coating process. This approach would begin with the application of a thin layer (< 1 μm) under high bias conditions, at 300 eV, followed by a subsequent deposition of a thicker layer (μm order) using an optimized bias that mitigates defect formation. The penetration depth of the RF field is approximately 40 nm for Nb [15], so only the surface of the second layer would be probed in RF applications, and any minor imperfections near the substrate are unlikely to cause substantial problems in cavity performance. Should this approach reveal that the defects induced by 300 eV ion bombardment negatively impact SRF cavity performance, the possibility of employing lower DC bias values for the planarization layer could be explored, even if it leads to less effective trench filling and planarity. Furthermore, it is important to recognize that the extreme nature of the substrate examined in this study is not representative of real-life cavities. In actual SRF cavities, most defects do not exhibit such sharp aspect ratios and are less susceptible to self-shadowing effects. Consequently, greater planarity can be expected in real scenarios across all ion energy levels under consideration.

The development of Nb films for SRF cavity applications engineered via a two-step approach for energetic condensation was already investigated through the Electron Cyclotron Resonance (ECR) plasma technique [65]. The controlled incoming ion energy was found to enable a number of processes such as desorption of adsorbed species, enhanced mobility of surface atoms and sub-implantation of impinging ions, allowing for improved film properties and enhanced adhesion to the substrate [66,67]. RF measurements on a Nb/Cu QPR sample coated with ECR in a two step process (first a nucleation phase of 100 nms performed at an ion energy of 184 eV, followed by deposition at 64 eV for the remainder of the film thickness) revealed an improved surface resistance at 4 K and 400 MHz when compared to an LHC-type coating [68]. The two step approach was also shown to improve the RF performance of ECR films, in opposition to keeping the ion energy high for the duration of the coating [69]. A similar process could be implemented with HiPIMS. A comprehensive investigation would be essential to determine the optimal bias value for achieving optimal planarization of the layer and, in parallel, an optimal bias value to minimize defect formation.

For this end, the crystalline and superconductive properties of the films need to be evaluated. A study is currently ongoing where crystalline defects are being quantitatively assessed and compared to the DC superconducting properties of the films. Impurities like oxygen, hydrogen, and krypton can potentially impact the residual resistance of the films and warrant further investigation. However, while bulk Nb suffers from hydrogen-induced Q-disease [70], Nb films (H content ~0.1 at% [71]) do not suffer from hydride formation, nor has hydrogen been found to be a major contributor to their residual resistance [16]. X-ray photoelectron spectroscopy (XPS) depth profiling on HiPIMS-deposited Nb films with DC substrate bias up to −400 V revealed only trace amounts of oxygen at the very surface of the Nb film (likely due to native oxide buildup), and that the oxygen at the Nb/Cu interface vanishes below the sensitivity level after the bakeout at 200 °C. Kr content was measured previously by excimer laser ablation and found to increase with bias voltage for ion bombardment energies up to −100 V. A detailed understanding of trapped Kr at higher ion bombardment energies, and of its relative importance to the residual resistance of the Nb films, requires additional measurements.

The dual-layer approach offers a promising solution for achieving both reduced stress and improved adhesion in Nb films. Higher ion bombardment energies leads to the creation of a sub-plantation layer of Nb on the Cu substrate, which is likely to improve adhesion [72]. No issues like film delamination were found so far (much more dependent on proper substrate surface treatment). Furthermore, while a slight increase was found for the film with the planarization layer deposited at −200 V, the films deposited at −300 V and −400 V exhibited lower residual stress compared to those deposited with the standard process. This aligns with literature on stress relaxation at higher energies [73]. Studies to explore the impact of the substrate surface state (e.g., impact of different surface treatments) on both the crystalline and superconducting properties of the films are being conducted. Finally, a separate investigation is underway to better understand the influence of the Cu substrate on the growth dynamics and the microstructure of the films [74].

6. Conclusion

Ionized sputtering using High Power Magnetron Sputtering (HiPIMS) combined with DC substrate biasing has been applied to the planarization of Nb films deposited on trenched Si substrates. The deposition of a flat Nb layer was achieved by HiPIMS with −300 V of DC bias. Film growth modeling predicted the planarization effect,

while also demonstrating that the increased normal incidence of the ionic incident flux plays a crucial role in achieving film planarization. Increased adatom mobility and re-sputtering, provided by the higher ion bombardment energies at higher bias values, proved experimentally to be vital for film planarization and densification. The results presented here reinforce the potential of HiPIMS, when combined with substrate biasing, to achieve flat and dense thin film layers on complex substrates when compared to conventional deposition methods. Furthermore, these results demonstrate the ability to mitigate the substrate's influence on the deposited layer by adjusting the applied bias value. As the propagation of macro defects like surface roughness from the substrate to the thin film is a source of performance degradation for Nb on Cu superconducting radiofrequency cavities, the attenuation of the latter could lead to a jump in their performance, making them better suited for future accelerators. This, in turn, could contribute significantly to improving the cost-effectiveness and sustainability of these machines.

CRediT authorship contribution statement

Carlota P.A. Carlos: Writing – review & editing, Writing – original draft, Visualization, Software, Investigation, Formal analysis, Data curation, Conceptualization. **Stewart Leith:** Writing – review & editing, Visualization, Investigation. **Guillaume Rosaz:** Writing – review & editing, Supervision, Investigation, Conceptualization. **Stephan Pfeiffer:** Writing – review & editing, Resources, Investigation. **Carmine Senatore:** Writing – review & editing, Supervision.

Declaration of competing interest

The authors declare that they have no known competing financial interests or personal relationships that could have appeared to influence the work reported in this paper.

Data availability

Data will be made available on request.

Acknowledgments

The research leading to this document is part of the Future Circular Collider study.

Appendix

The schematic diagram of the sputtering system is presented in Fig. 10(a). The UHV chamber was mounted around a cylindrical cathode and insulated from it and from the ground using two ceramic vacuum breaks, Fig. 10(2a) and (2b), respectively. Coupled to them, two small chambers equipped with a CF-DN16 port are then used to connect the anodes. A DN40 port is used on the lower chamber to connect a non-evaporable getter (NEG) pump (Fig. 10(5). At the bottom of the system, an angle valve (Fig. 10(6)) does the connection to the ultrahigh vacuum pumping group, also equipped with injection valves for the process gas.

Fig. 10(b) shows a cross section view of the setup. The inset, Fig. 10(c), highlights the cathode assembly. The latter is made of a 38 mm external diameter stainless steel tube (Fig. 10(11), highlighted in green), closed at its lower extremity and welded to the cathode top flange (Fig. 10(1)). A central cylindrical electrode, made of pure Nb with 45 mm external diameter (Fig. 10(10), highlighted in dark blue), is in direct contact with the stainless steel tube. Two cylindrical Al_2O_3 ceramics (Fig. 10(8), highlighted in red) are used as electrical insulators between the central tube and the upper and lower anodes (Fig. 10, (9a) and (9b) respectively, highlighted in light blue). These electrodes, of 53 mm external diameter, are also made of pure Nb. The upper and lower electrodes are electrically connected using type-N UHV connectors (Fig. 10(7a) and (7b) respectively). The three electrodes can thus be independently connected either to a power supply or to the ground.

When coating, the central electrode is connected to the power supply and the upper and lower electrodes are kept at ground potential. This means that the latter act as anodes during the plasma discharge, allowing the electron current to flow out of the system and the chamber to be biased at any desired potential. The magnetic field necessary for sustaining the magnetron discharge is provided by a cylindrical permanent NdFeB (N45SH) magnet (50 mm in length, 30 mm external diameter and 10 mm internal diameter). A flow of compressed air in the

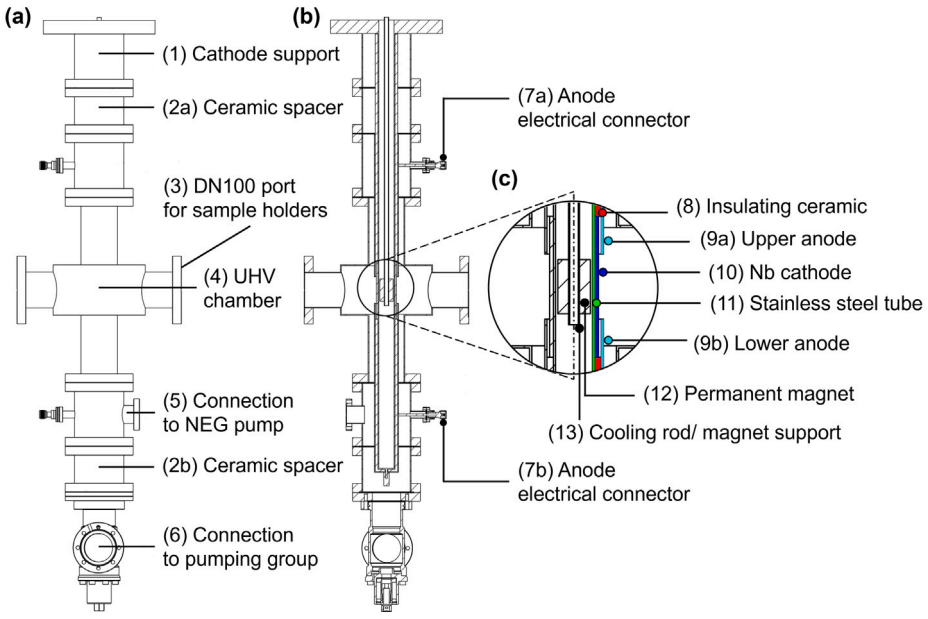

Fig. 10. Schematic representation (a) and cross section view (b) of the coating apparatus used to deposit Nb into the trenched Si samples. The inset (c) highlights the cathode assembly.

tube cools down the magnet and prevents its demagnetization during the coating process.

References

[1] O. Brüning, S. Myers, Challenges and Goals for Accelerators in the XXI Century, World Scientific, 2016, http://dx.doi.org/10.1142/8635.

[2] F. Zimmermann, Accelerators in the 21st century, in: Y. Aharonov, L. Bravina, S. Kabana (Eds.), EPJ Web Conf. 182 (2018) 02134, http://dx.doi.org/10.1051/epjconf/201818202134.

[3] The EuCARD-2 Collaboration, Applications of Particle Accelerators in Europe, Tech. Rep., CERN, Geneva, 2017, URL http://cds.cern.ch/record/2716155.

[4] M. Dosanjh, From particle physics to medical applications, in: From Particle Physics to Medical Applications, 2399-2891, IOP Publishing, 2017, pp. 1–21, http://dx.doi.org/10.1088/978-0-7503-1444-2ch1.

[5] N. Mounet (Ed.), European Strategy for Particle Physics - Accelerator R&D Roadmap, vol. 1, Monographs, CERN, Geneva, CERN YellowReports, 2022, http://dx.doi.org/10.23731/CYRM-2022-001.

[6] S.V. Kutsaev, Advanced technologies for applied particle accelerators and examples of their use (review), Tech. Phys. 66 (2) (2021) 161–195, http://dx.doi.org/10.1134/s1063784221020158.

[7] Y. Wang, D. Chen, R. dos Santos Augusto, J. Liang, Z. Qin, J. Liu, Z. Liu, Production review of accelerator-based medical isotopes, Molecules 27 (16) (2022) 5294, http://dx.doi.org/10.3390/molecules27165294.

[8] R.C. Dhuley, I. Gonin, S. Kazakov, T. Khabiboulline, A. Sukhanov, V. Yakovlev, A. Saini, N. Solyak, A. Sauers, J.C.T. Thangaraj, K. Zeller, B. Coriton, R. Kostin, Design of a 10 MeV, 1000 kW average power electron-beam accelerator for wastewater treatment applications, Phys. Rev. Accel. Beams 25 (4) (2022) 041601, http://dx.doi.org/10.1103/physrevaccelbeams.25.041601.

[9] J. Golm, S. Arguedas Cuendis, S. Calatroni, C. Cogollos, B. Döbrich, J. Gallego, J.M. García Barceló, X. Granados, J. Gutierrez, I.G. Irastorza, T. Koettig, N. Lamas, J. Liberadzka-Porret, C. Malbrunot, W.L. Millar, P. Navarro, C.P.A. Carlos, T. Puig, G.J. Rosaz, M. Siodlaczek, G. Telles, W. Wuensch, Thin film (high temperature) superconducting radiofrequency cavities for the search of axion dark matter, IEEE Trans. Appl. Supercond. 32 (4) (2022) 1–5, http://dx.doi.org/10.1109/tasc.2022.3147741.

[10] A. Romanenko, R. Pilipenko, S. Zorzetti, D. Frolov, M. Awida, S. Belomestnykh, S. Posen, A. Grassellino, Three-dimensional superconducting resonators at $T <$ 20 mK with photon lifetimes up to $\tau = 2$, Phys. Rev. A 13 (3) (2020) 034032, http://dx.doi.org/10.1103/physrevapplied.13.034032.

[11] M. Benedikt, A. Blondel, O. Brunner, M. Capeans Garrido, F. Cerutti, J. Gutleber, P. Janot, J.M. Jimenez, V. Mertens, A. Milanese, K. Oide, J.A. Osborne, T. Otto, Y. Papaphilippou, J. Poole, L.J. Tavian, F. Zimmermann, FCC-EE: The lepton collider: Future circular collider conceptual design report volume 2, Eur. Phys. J. Spec. Top. 228 (2) (2019) 261–623, http://dx.doi.org/10.1140/epjst/e2019-900045-4.

[12] FCC energy efficiency, https://fcc.web.cern.ch/energy-efficiency. (Accessed 29 November 2023).

[13] A. Grassellino, A. Romanenko, Y. Trenikhina, M. Checchin, M. Martinello, O.S. Melnychuk, S. Chandrasekaran, D.A. Sergatskov, S. Posen, A.C. Crawford, S. Aderhold, D. Bice, Unprecedented quality factors at accelerating gradients up to 45 MVm^{-1} in niobium superconducting resonators via low temperature nitrogen infusion, Supercond. Sci. Technol. 30 (9) (2017) 094004, http://dx.doi.org/10.1088/1361-6668/aa7afe.

[14] D. Bafia, A. Grassellino, O. Melnychuk, A. Romanenko, Z.-H. Sung, J. Zasadzinski, Gradients of 50 MV/m in TESLA shaped cavities via modified low temperature bake, in: Proceedings of the 19th International Conference on RF Superconductivity, vol. SRF2019, JACoW Publishing, Geneva, Switzerland, Germany, 2019, http://dx.doi.org/10.18429/JACOW-SRF2019-TUP061.

[15] A.-M. Valente-Feliciano, Superconducting RF materials other than bulk niobium: A review, Supercond. Sci. Technol. 29 (11) (2016) 113002, http://dx.doi.org/10.1088/0953-2048/29/11/113002.

[16] C. Benvenuti, S. Calatroni, I.E. Campisi, P. Darriulat, M.A. Peck, R. Russo, A.-M. Valente, Study of the surface resistance of superconducting niobium films at 1.5 GHz, Physica C 316 (3–4) (1999) 153–188, http://dx.doi.org/10.1016/s0921-4534(99)00207-5.

[17] H. Padamsee, The science and technology of superconducting cavities for accelerators, Supercond. Sci. Technol. 14 (4) (2001) R28–R51, http://dx.doi.org/10.1088/0953-2048/14/4/202.

[18] J.P.H. Sladen, Status of superconducting cavities in LEP, Part. Accel. 60 (1997) 15–25. 6 p, URL https://cds.cern.ch/record/343059.

[19] D. Boussard, E. Chiaveri, E. Haebel, H.P. Kindermann, R. Losito, S. Marque, V. Rodel, M. Stirbet, The LHC superconducting cavities, in: Proceedings of the 1999 Particle Accelerator Conference (Cat. No.99CH36366), vol. 2, IEEE, New York, NY, USA, 1999, pp. 946–948, http://dx.doi.org/10.1109/pac.1999.795409.

[20] W. Venturini Delsolaro, S. Calatroni, B. Delaup, A. D'Elia, N.M. Jecklin, Y. Kadi, G. Keppel, D. Lespinasse, P. Maesen, I. Mondino, V. Palmieri, S. Stark, A.R.M. Sublet, M. Therasse, Nb sputtered quarter wave resonators for the HIE-ISOLDE, in: Proc. SRF'13, in: 16th International Conference on RF Superconductivity, JACoW, Paris, France, 2013, p. WEIOA03, URL https://cds.cern.ch/record/2062217.

[21] G. Bisoffi, G. Bassato, S. Canella, D. Carlucci, A. Facco, P. Modanese, A. Pisent, A.M. Porcellato, P.A. Posocco, ALPI QWR and S-RFQ operating experience, in: Proc. SRF'07, in: 13th International Conference on RF Superconductivity, Peking Univ., Beijing, China, 2007, p. 55.

[22] S. Calatroni, 20 Years of experience with the Nb/Cu technology for superconducting cavities and perspectives for future developments, Physica C 441 (1–2) (2006) 95–101, http://dx.doi.org/10.1016/j.physc.2006.03.044.

[23] F. Peauger, O. Brunner, The SRF system options for FCC-EE, 2023, FCC week London 2023.

[24] W. Venturini Delsolaro, M. Garlasche, F. Peauger, G. Rosaz, I. Karpov, L. Zhang, A.M. Valente Feliciano, S.A. Udongwo, A. Bianchi, G. Bellini, L.M.A. Ferrera, C. Pereira Carlos, L. Vega Cid, S. Leith, T. Proslier, S. Gorgi Zadeh, M. Timmins, M. Therasse, T. Koettig, S. Atieh, O. Brunner, F. Gerigk, Progress and R&D challenges for FCC-EE SRF, EPJ Tech. Instrum. 10 (1) (2023) http://dx.doi.org/10.1140/epjti/s40485-023-00094-5.

[25] C. Benvenuti, P. Bernard, D. Bloess, G. Cavallari, E. Chiaveri, E. Haebel, N. Hilleret, J. Tuckmantel, W. Weingarten, Superconducting niobium sputter-coated copper cavity modules for the LEP energy upgrade, in: Conference Record of the 1991 IEEE Particle Accelerator Conference, IEEE, 1991, pp. 1023–1025, http://dx.doi.org/10.1109/pac.1991.164525.

[26] S. Bauer, W. Diete, B. Griep, M. Peiniger, H. Vogel, P. vom Stein, S. Calatroni, E. Chiaveri, R. Losito, Production of Nb/Cu sputtered superconducting cavities for LHC, in: Proc. SRF'99, in: 9th Workshop on RF Superconductivity, Santa Fe, New Mexico, USA, 1999, p. WEP016, URL https://accelconf.web.cern.ch/SRF99/papers/wep016.pdf.

[27] C. Benvenuti, D. Boussard, J. Tückmantel, S. Calatroni, E. Chiaveri, Production and test of 352 MHz niobum-sputtered reduced–β cavities, in: Proc. SRF'97, in: 8th Workshop on RF Superconductivity, Abano-Terme, Italy, 1997, pp. 1038–1049, URL https://cds.cern.ch/record/343064.

[28] C. Benvenuti, S. Calatroni, P. Darriulat, M.A. Peck, A.-M. Valente, C.A.V. Hof, Study of the residual surface resistance of niobium films at 1.5 GHz, Physica C 351 (4) (2001) 421–428, http://dx.doi.org/10.1016/s0921-4534(00)01645-2.

[29] A. Miyazaki, W.V. Delsolaro, Two different origins of the Q-slope problem in superconducting niobium film cavities for a heavy ion accelerator at CERN, Phys. Rev. Accel. Beams 22 (7) (2019) 073101, http://dx.doi.org/10.1103/physrevaccelbeams.22.073101.

[30] F. Avino, D. Fonnesu, T. Koettig, M. Bonura, C. Senatore, A.T.P. Fontenla, A. Sublet, M. Taborelli, Improved film density for coatings at grazing angle of incidence in high power impulse magnetron sputtering with positive pulse, Thin Solid Films 706 (2020) 138058, http://dx.doi.org/10.1016/j.tsf.2020.138058.

[31] M. Arzeo, F. Avino, S. Pfeiffer, G. Rosaz, M. Taborelli, L. Vega-Cid, W. Venturini-Delsolaro, Enhanced radio-frequency performance of niobium films on copper substrates deposited by high power impulse magnetron sputtering, Supercond. Sci. Technol. 35 (5) (2022) 054008, http://dx.doi.org/10.1088/1361-6668/ac5646.

[32] L. Vega-Cid, S. Atieh, L.M.A. Ferreira, L. Laín-Amador, S.B. Leith, C.P. Carlos, G.J. Rosaz, K. Scibor, W.V. Delsolaro, P.V. Garcia, Seamless 1.3 GHz copper cavities for Nb coatings: Cold test results of two different approaches, in: Proc. SRF'21, in: 20th International Conference on RF Superconductivity, JACoW Publishing, Geneva, Switzerland, 2022, pp. 498–502, http://dx.doi.org/10.18429/JACoW-SRF2021-TUPTEV009, URL https://jacow.org/srf2021/papers/tuptev009.pdf.

[33] C.P.A. Carlos, S. Leith, G. Rosaz, M. Taborelli, M. Bonura, C. Senatore, S. Pfeiffer, A.T.P. Fontenla, G. Bellini, L. Ferreira, L. Vega-Cid, A. Bianchi, W. Venturini-Delsolaro, T. Proslier, Y. Kalbouss, HiPIMS Nb coatings: From 1.3 GHz to 400 MHz, 2023, FCC week, London 2023.

[34] I.O. Kulik, V. Palmieri, Theory of Q-degradation and nonlinear effects in Nb-coated superconducting cavities, Part. Accel. 60 (1998) 257–264.

[35] Y. Homma, S. Tsunekawa, Planar deposition of aluminum by RF/DC sputtering with RF bias, J. Electrochem. Soc. 132 (6) (1985) 1466–1472, http://dx.doi.org/10.1149/1.2114145.

[36] B.W. Kempshall, S.M. Schwarz, B.I. Prenitzer, L.A. Giannuzzi, R.B. Irwin, F.A. Stevie, Ion channeling effects on the focused ion beam milling of Cu, J. Vac. Sci. Technol. B 19 (3) (2001) 749–754, http://dx.doi.org/10.1116/1.1368670.

[37] NASCAM, http://www.unamur.be/sciences/physique/pmr/telechargement/logiciels/nascam. (Accessed 29 November 2023).

[38] S. Lucas, P. Moskovkin, Simulation at high temperature of atomic deposition, islands coalescence, Ostwald and inverse Ostwald ripening with a general simple kinetic Monte Carlo code, Thin Solid Films 518 (18) (2010) 5355–5361, http://dx.doi.org/10.1016/j.tsf.2010.04.064.

[39] P. Moskovkin, S. Lucas, Computer simulations of the early-stage growth of Ge clusters at elevated temperatures on patterned Si substrate using the kinetic Monte Carlo method, Thin Solid Films 536 (2013) 313–317, http://dx.doi.org/10.1016/j.tsf.2013.03.031.

[40] A. Anders, A structure zone diagram including plasma-based deposition and ion etching, Thin Solid Films 518 (15) (2010) 4087–4090, http://dx.doi.org/10.1016/j.tsf.2009.10.145.

[41] J.A. Thornton, Influence of apparatus geometry and deposition conditions on the structure and topography of thick sputtered coatings, J. Vac. Sci. Technol. 11 (4) (1974) 666–670, http://dx.doi.org/10.1116/1.1312732.

[42] J. Dervaux, P.A. Cormier, P. Moskovkin, O. Douheret, S. Konstantinidis, R. Lazzaroni, S. Lucas, R. Snyders, Synthesis of nanostructured Ti thin films by combining glancing angle deposition and magnetron sputtering: A joint experimental and modeling study, Thin Solid Films 636 (2017) 644–657, http://dx.doi.org/10.1016/j.tsf.2017.06.006.

[43] Y. Kudriavtsev, A. Villegas, A. Godines, R. Asomoza, Calculation of the surface binding energy for ion sputtered particles, Appl. Surf. Sci. 239 (3–4) (2005) 273–278, http://dx.doi.org/10.1016/j.apsusc.2004.06.014.

[44] SIMTRA, https://www.ugent.be/we/solidstatesciences/draft/en/services/software. (Accessed 29 November 2023).

[45] K. VanAeken, S. Mahieu, D. Depla, The metal flux from a rotating cylindrical magnetron: A Monte Carlo simulation, J. Phys. D: Appl. Phys. 41 (20) (2008) 205307, http://dx.doi.org/10.1088/0022-3727/41/20/205307.

[46] D. Depla, W.P. Leroy, Magnetron sputter deposition as visualized by Monte Carlo modeling, Thin Solid Films 520 (20) (2012) 6337–6354, http://dx.doi.org/10.1016/j.tsf.2012.06.032.

[47] SRIM, http://www.srim.org/. (Accessed 29 November 2023).

[48] J.F. Ziegler, M.D. Ziegler, J.P. Biersack, SRIM – the stopping and range of ions in matter (2010), Nucl. Instrum. Methods Phys. Res. B 268 (11–12) (2010) 1818–1823, http://dx.doi.org/10.1016/j.nimb.2010.02.091.

[49] S. Rauf, Effect of bias voltage waveform on ion energy distribution, J. Appl. Phys. 87 (11) (2000) 7647–7651, http://dx.doi.org/10.1063/1.373435.

[50] T. Baloniak, R. Reuter, A. von Keudell, Fundamental aspects of substrate biasing: Ion velocity distributions and nonlinear effects, J. Phys. D: Appl. Phys. 43 (33) (2010) 335201, http://dx.doi.org/10.1088/0022-3727/43/33/335201.

[51] G. Greczynski, J. Jensen, L. Hultman, Mitigating the geometrical limitations of conventional sputtering by controlling the ion-to-neutral ratio during high power pulsed magnetron sputtering, Thin Solid Films 519 (19) (2011) 6354–6361, http://dx.doi.org/10.1016/j.tsf.2011.04.031.

[52] S. Mahieu, K.V. Aeken, D. Depla, Transport of sputtered particles through the gas phase, in: Reactive Sputter Deposition, Springer Berlin Heidelberg, 2008, p. 210, http://dx.doi.org/10.1007/978-3-540-76664-3_6.

[53] A. Anders, J. Andersson, A. Ehiasarian, High power impulse magnetron sputtering: Current-voltage-time characteristics indicate the onset of sustained self-sputtering, J. Appl. Phys. 102 (11) (2007) 113303, http://dx.doi.org/10.1063/1.2817812.

[54] U. Helmersson, M. Lattemann, J. Bohlmark, A.P. Ehiasarian, J.T. Gudmundsson, Ionized physical vapor deposition (IPVD): A review of technology and applications, Thin Solid Films 513 (1–2) (2006) 1–24, http://dx.doi.org/10.1016/j.tsf.2006.03.033.

[55] A. Butler, N. Brenning, M.A. Raadu, J.T. Gudmundsson, T. Minea, D. Lundin, On three different ways to quantify the degree of ionization in sputtering magnetrons, Plasma Sources. Sci. Technol. 27 (10) (2018) 105005, http://dx.doi.org/10.1088/1361-6595/aae05b.

[56] T. Kozák, J. Vlček, Š. Kos, Transport and ionization of sputtered atoms in high-power impulse magnetron sputtering discharges, J. Phys. D: Appl. Phys. 46 (10) (2013) 105203, http://dx.doi.org/10.1088/0022-3727/46/10/105203.

[57] C. Huo, D. Lundin, M.A. Raadu, A. Anders, J.T. Gudmundsson, N. Brenning, On the road to self-sputtering in high power impulse magnetron sputtering: Particle balance and discharge characteristics, Plasma Sources. Sci. Technol. 23 (2) (2014) 025017, http://dx.doi.org/10.1088/0963-0252/23/2/025017.

[58] J.T. Gudmundsson, D. Lundin, N. Brenning, M.A. Raadu, C. Huo, T.M. Minea, An ionization region model of the reactive Ar/O_2 high power impulse magnetron sputtering discharge, Plasma Sources. Sci. Technol. 25 (6) (2016) 065004, http://dx.doi.org/10.1088/0963-0252/25/6/065004.

[59] M. Hála, J. Čapek, O. Zabeida, J.E. Klemberg-Sapieha, L. Martinu, Pulse management in high power pulsed magnetron sputtering of niobium, Surf. Coat. Technol. 206 (19–20) (2012) 4186–4193, http://dx.doi.org/10.1016/j.surfcoat.2012.04.019.

[60] J. Čapek, M. Hála, O. Zabeida, J.E. Klemberg-Sapieha, L. Martinu, Deposition rate enhancement in HiPIMS without compromising the ionized fraction of the deposition flux, J. Phys. D: Appl. Phys. 46 (20) (2013) 205205, http://dx.doi.org/10.1088/0022-3727/46/20/205205.

[61] G. Terenziani, S. Calatroni, A.P. Ehiasarian, Niobium coatings for superconducting RF applications by HIPIMS, in: Proceedings 4th International Conference on Fundamentals and Industrial Applications of HIPIMS: Braunschweig, 2012, p. 16, http://dx.doi.org/10.13140/2.1.2837.9846.

[62] J.T. Gudmundsson, N. Brenning, D. Lundin, U. Helmersson, High power impulse magnetron sputtering discharge, J. Vac. Sci. Technol. A 30 (3) (2012) 030801, http://dx.doi.org/10.1116/1.3691832.

[63] S. Leith, Development of Novel Superconducting Thin Films for Use in Superconducting Radio Frequency Cavities (Ph.D. thesis), Universität Siegen, Siegen, 2021, p. 157, http://dx.doi.org/10.25819/ubsi/10031, URL https://dspace.ub.uni-siegen.de/handle/ubsi/2108.

[64] L. Jablonka, P. Moskovkin, Z. Zhang, S.-L. Zhang, S. Lucas, T. Kubart, Metal filling by high power impulse magnetron sputtering, J. Phys. D: Appl. Phys. 52 (36) (2019) 365202, http://dx.doi.org/10.1088/1361-6463/ab28e2.

[65] G. Wu, A.M. Valente, H.L. Phillips, H. Wang, A.T. Wu, T.J. Renk, P. Provencio, Studies of niobium thin film produced by energetic vacuum deposition, Thin Solid Films 489 (1–2) (2005) 56–62, http://dx.doi.org/10.1016/j.tsf.2005.04.099.

[66] A.M. Valente-Feliciano, Nb films: Substrates, nucleation & crystal growth, in: Proc. SRF'11, in: 15th International Conference on RF Superconductivity, 2011, pp. 332–342, URL https://www.osti.gov/biblio/1994829.

[67] A.-M. Valente-Feliciano, Development of SRF Monolayer/Multilayer Thin Film Materials to Increase the Performance of SRF Accelerating Structures beyond Bulk Nb (Ph.D. thesis), (2014PA112254) Université Paris Sud - Paris XI, 2014, URL https://theses.hal.science/tel-01126883.

[68] A.-M. Valente-Feliciano, S. Aull, G. Eremeev, T. Proslier, C. Reece, J. Spradlin, Material quality & SRF performance of Nb films grown on Cu via ECR plasma energetic condensation, in: Proc. SRF'15, in: 17th International Conference on RF Superconductivity, 2015, pp. 622–625, http://dx.doi.org/10.18429/JACoW-SRF2015-TUPB029, URL http://cds.cern.ch/record/2288264.

[69] A.M. Valente-Feliciano, G.V. Eremeev, J.K. Spradlin, H.L. Phillips, C.E. Reece, C. Cao, T. Proslier, T. Tao, ECR Nb films grown on amorphous and crystalline Cu substrates: Influence of ion energy, in: Proc. SRF'13, in: 16th International Conference on RF Superconductivity, 2013, pp. 631–634, URL https://www.osti.gov/biblio/1121266.

[70] B. Bonin, R.W. Roth, Q degradation of niobbium cavities due to hydrogen contamination, Part. Accel. 40 (1992) 59–83.

[71] C. Benvenuti, S. Calatroni, M. Hakovirta, H. Neupert, M. Prada, A.M. Valente, CERN studies on niobium-coated 1.5 GHz copper cavities, in: The 10th Workshop on RF Superconductivity, 2001, Tsukuba, Japan, 2001, URL https://cds.cern.ch/record/572633/files/est-2002-004.pdf.

[72] A.M. Valente-Feliciano, HIPIMS: A new generation of film deposition techniques for srf applications, in: Proc. SRF'13, in: 16th International Conference on RF Superconductivity, 2013, pp. 754–760, URL https://accelconf.web.cern.ch/srf2013/papers/weioa01.pdf.

[73] M.M.M. Bilek, D.R. McKenzie, A comprehensive model of stress generation and relief processes in thin films deposited with energetic ions, Surf. Coat. Technol. 200 (14–15) (2006) 4345–4354, http://dx.doi.org/10.1016/j.surfcoat.2005.02.161.

[74] M. Ghaemi, A. Lopez-Cazalilla, K. Sarakinos, G.J. Rosaz, C.P.A. Carlos, S. Leith, S. Calatroni, M. Himmerlich, F. Djurabekova, Growth of Nb films on Cu for superconducting radio frequency cavities by direct current and high power impulse magnetron sputtering: A molecular dynamics and experimental study, Surf. Coat. Technol. 476 (2024) 130199, http://dx.doi.org/10.1016/j.surfcoat.2023.130199.